Stray Light and Thermal Self-Emission Minimization at the ELT

Ronald Holzlöhner*, Johan Kosmalski, Stéphane Guisard
European Southern Observatory, Karl-Schwarzschild Straße 2, D-85748 Garching, Germany

ABSTRACT

We analyze the principal sources of thermal self-emission (TSE) in the European Southern Telescope (ELT) as they will be seen by the instruments observing in the infrared. Expected TSE levels for different mirror contamination levels and instrument cold stop types are provided.

Keywords: Stray light, thermal self-emission, mirror contamination, dust, scattering

1. INTRODUCTION

We define stray light as any unwanted light in an optical system. Stray light in the ELT *relevant to astronomy* can be classified into different categories, as attempted in Fig. 1. This work covers Thermal Self-Emission (TSE).

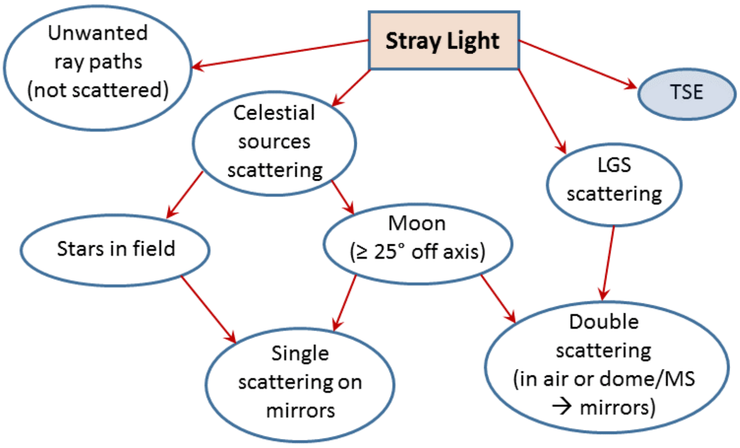

Figure 1. Classification of stray light relevant to ELT science (LGS = laser guide stars; MS = Main (telescope) Structure). This work covers Thermal Self-Emission (TSE).

1.1 Radiometric Energy Balance

In order to analyze the thermal radiation in telescopes, it is instructive to discuss the laws governing radiation balance on any surface at a fixed wavelength [5]

$$\alpha + \rho + t = 1, \tag{1}$$

where

α = absorptivity is the fraction of radiation power absorbed by a surface,

ρ = reflectivity is the fraction reflected by the surface,

t = transmissivity is the fraction transmitted by the surface.

*rholzloe[at]eso.org; phone +49-89-3200-6671; eso.org

On an opaque surface like a mirror or a dome/MS structural part, $t = 0$. Further, Kirchhoff's Law of thermal radiation states

$$\alpha = \varepsilon, \qquad i = \varepsilon\, i_{bb}, \tag{2}$$

where ε is the emissivity, hence the fraction of thermal irradiance i emitted from a surface relative to the thermal spectral irradiance $i_{bb} = i_{bb}(\lambda, T)$ emitted by a black body at a wavelength λ and temperature T (the functional form of $i_{bb}(\lambda, T)$ is given by Planck's law and not reproduced here explicitly). Combining Eqs.(1) and (2), we find the simple relationship $\rho(\lambda) + \varepsilon(\lambda) = 1$ for any opaque surface. In other words, the sum of reflected and thermally emitted irradiance from any surface in any direction and wavelength equals unity.

The wavelength-dependent reflectivity can be decomposed into specular and scattered components as $\rho(\lambda) = \rho_{\text{spec}}(\lambda) + \rho_{\text{scat}}(\lambda)$. In the case of a telescope mirror, the specular reflectivity normally applies to radiation from the (cold) sky when viewed from the detector. By contrast, light from any direction on sky, or else the (warm) telescope structure or the dome, can scatter off a mirror and arrive at the detector. Therefore, a significant fraction of scattered light actually originates from warm surfaces and is simply relayed by dust or roughness on a mirror (depending on the solid angles under which the mirror sees warm surfaces and the scatter BSDF on its surface). One can make the conservative approximation

$$\varepsilon(\lambda) \approx 1 - \rho_{\text{spec}}(\lambda), \tag{3}$$

in ground-based telescopes.

The Law of Stefan and Boltzmann dictates further that the total thermal irradiance I_{bb} emitted by a perfectly black body, obtained by integrating $i_{bb}(\lambda, T)$ over all wavelengths, obeys

$$I_{bb} = \sigma\, T^4, \qquad \sigma = 5.67 \times 10^{-8}\ \frac{W}{m^2 K^4}\ , \tag{4}$$

where σ is the Stefan-Boltzmann constant and T is the absolute temperature of the surface (i.e., in Kelvin). As a consequence, all surfaces in a system that is in thermal equilibrium radiate equally and it is impossible to detect any contrast, in accordance with the Second Law of Thermodynamics (e.g., when looking into a pottery oven whose content is in red heat, one needs an outside light source to distinguish any objects). Applied to a telescope in Paranal at night, one finds that any part of the dome or main structure in thermal equilibrium with the air radiates $I_{bb} = \sigma T_{\text{air}}^4$, where $T_{\text{air}} \approx (273 + 14)$ K.

1.2 Night Sky Radiance

When the dome is open, the telescope mirrors and detectors differ from the situation described in the preceding subsection in that they look at the cold (night) sky which is not in thermal equilibrium with the dome. The effective background temperature of the universe at present is about 2.7 K. However, the thermal radiance seen by ground-based telescopes is dominated by the thermal radiation of the atmosphere and depends strongly on wavelength.

Figure 2 shows in the blue curves a plot of night sky radiance at Paranal for airmass 1.25 (37˚ zenith angle) with a Moon/object separation angle of 45˚ and half Moon from SkyCalc. The astronomical bands are indicated in amber.

The green curves represents Planck's formula of black body radiance at 14ºC and 6ºC; $i_{bb}(\lambda, T = (273 + 14)K)$ and $i_{bb}(\lambda, T = (273 + 6)K)$, respectively. The temperature of 14ºC is close to the median Paranal nighttime ground temperature (the median temperature on top of Cerro Armazones, the site of the ELT, is 9 ºC). The blue curve shows where the atmosphere becomes transparent and windows open up for terrestrial astronomical observation in the infrared (e.g., the well-known "water window" in N-band). An overview of atmospheric emission bands is shown in Fig.10 (Appendix).

The effective night sky temperature with clear skies lies below 14˚ C and black/gray bodies that can see a significant solid angle of the (Paranal) night sky experience radiative cooling. During a clear night in the desert with a ground air temperature of 14°C and a relative humidity of 15%, detailed atmospheric models [7, p.77; 4] yield a sky thermal irradiance of about 220 W/m^2 (radiation from the hemispherical sky onto a horizontal surface), which in turn corresponds to an effective sky black body temperature of about −23°C. The effective night sky temperature on Cerro Armazones with clear skies is not fixed and lies roughly −32 K below the ambient ground temperature, hence the curves in Fig. 2 can be scaled to other ambient temperatures.

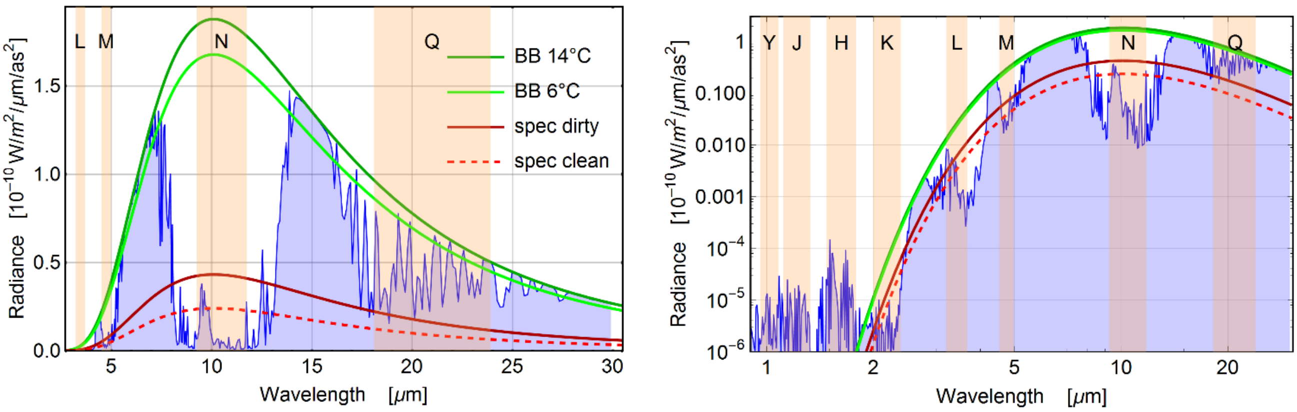

Figure 2. Blue: Night sky spectral radiance from SkyCalc in linear and logarithmic scales. Green curve: Black body radiance $i_{bb}(\lambda, T)$ for 14 ºC and 6 ºC, solid red: 0.23 × $i_{bb}(\lambda, T)$, (spec dirty mirrors 14ºC), red dashed: 0.128 × $i_{bb}(\lambda, T)$ (clean mirror)

The night sky radiation has a number of additional spectral components included by SkyCalc: Scattered Moonlight, scattered starlight, Zodiacal light (scattered light from interplanetary dust), molecular emission of the lower and upper atmosphere and airglow (recombination of photoionized atoms, luminescence caused by cosmic rays, chemiluminescence etc.). However, these components are appreciable only from the visible to K-band.

Table 1 shows an overview of the sky radiance at New Moon in the astronomical bands from the ultraviolet to the far IR in units of photon flux, in-band magnitudes and radiance [W/m^2/as^2]. The last column indicates the fraction of 12.8% of the black body radiation, equaling the maximum allowed thermal telescope emission set in INFO-INS/ELT-195 of the Common ICD [20] for perfectly clean mirrors, evaluated at 14˚C. The same emission is plotted in Fig. 2 in the dashed red curve. The solid red curve indicates the TSE limit in the presence of mirror contamination (23% emissivity).

From Table 1 and Fig. 2 it becomes clear that the telescope thermal emissivity) in the K, L and N bands lies far above the sky background and thus dominates the achievable signal-to-noise ratio (SNR). Therefore, low telescope emissivity is crucial at observing wavelengths above 1 micron.

Table 1: Sky radiance for various astronomical bands at New Moon (λcen: center wavelength, Δλ: width). Last column: Ratio of thermal radiance spec at 14˚C to sky radiance

Band	λ_{cen} [nm]	$\Delta\lambda$ [nm]	Sky Radiance [ph/s/m^2/as^2]	mag	Sky Radiance [10^{-12} W/m^2/as^2]	(0.128 × I_{bb} (14°C)) × Sky Radiance^{-1}
U	365	66	8.06	22	4.42e−6	4.5e−42
B	445	94	11.9	22.6	5.33e−6	6.4e−32
V	551	88	20.5	21.6	7.32e−6	1.2e−24
R	658	138	38.4	21	1.17e−5	1.8e−18
I	806	149	121	19.4	2.94e−5	7.3e−14
Y	1020	120	394	17.4	7.65e−5	5.5e−10
J	1220	213	1080	16.5	1.75e−4	6.7e−7
H	1630	307	6360	14.2	7.86e−4	0.001
K	2190	390	2150	14.8	1.96e−4	2.1
L	3450	472	2.5e6	–	0.148	1.2
M	4750	460	7.12e7	–	2.98	0.6
N	10 500	2500	1.38e9	–	27.7	2.1
Q	21 000	5800	2.99e10	–	285	0.19

1.3 Emissivity of Surfaces

Any warm surface whose radiation can reach the focal plane of an instrument working in the IR will degrade the SNR. In the remainder of this document, it will be assumed that the instruments employ cold stops that block all radiation not coming from the telescope pupil (the precise definition of the pupil will be discussed in the next section). The central obscuration and the spider shall be masked.

The thermal emissivity that remains stems from three types of sources:

1. Mirror discontinuities, namely M1 intersegment gaps and missing segments,
2. imperfect intrinsic mirror reflectivity (i.e., ohmic dissipation in the metallic coatings, described by the imaginary part of the refractive indices of the coating layers) and
3. dust on mirrors (both emits and scatters thermal radiation).

The thermal emission of any surface that is seen from the science detectors through the cold stop can be lowered in principle by cooling and/or lowering its emissivity, thus raising its reflectivity. Since temperature differences inside the dome induce local turbulence, the first option is ruled out. Raising the reflectivity of surfaces in, or near, the science light beam is risky since it may induce scattering and thus raise the stray light level, in particular in the UV and visible. Ideal would be a material that is black in the visible but highly reflective in the IR. Such a is sold under the name *NanoBlack* on self-adhesive foils by the company Acktar. A spectral reflectance chart is reproduced in Fig. 9 in the Appendix.

At the time of writing, ESO is investigating options for a modified *NanoBlack* foil whose low emissivity also covers K-band.

Wrapping a section of a telescope structure in such foil that is exposed to a large solid angle of the sky has the advantage that the radiative cooling is strongly reduced, while suppressing visible stray light. On surfaces that can be directly or indirectly seen by IR instruments (e.g., the underside of a spider vane or of the M2 crown), it lowers thermal emission. Note that these latter structure sections are also subject to sky cooling since they see a large fraction of the sky through M1.

1.4 Scattering on Dusty Mirrors

Dust on mirrors deserves special attention. The scattering on a single grain of dust, which consists mostly of minerals like silicon dioxide, is well described by Mie scatter theory [3]. On a mirror, things become more complicated since the particles cover a wide range of sizes and most of the light scattered by the particle is actually reflected by the mirror. In general, the larger the particle, the more light will be scattered into narrow cone centered along the incident light rays. The ensemble of particles acts like an isotropic random 2D grating. The vast majority of the scattered light off a dusty mirror is hence emerging near the specular reflection. The angle-dependent scattered light intensity is described by the Bidirectional Scatter Distribution Function (BSDF) [15].

When light falls onto a dust particle, some of it scatters elastically (i.e., radiation is redirected), but also there is dissipative absorption, described by the imaginary component of the particle's refractive index. The combined cross section of scattering and absorption equals about twice the geometrical cross section of the particle, a rule known as the Extinction Paradox [3]. However, the larger the particle compared to the wavelength, the closer the majority of the scattered light will point along the incident rays and only be distinguishable from the unscattered light in the far field. In the case of a telescope, this means that while scattering will add stray light anywhere in the focal plane, it specifically also broadens the PSF which reduces contrast and complicates exoplanet detection.

Tables 2 list the Total Integrated Scattering (TIS) and Total Integrated Absorption (TIA) for PAC = 1% geometrical dust area coverage on a surface. The table on the left is for the lognormal particle size distribution slope of 0.926, which corresponds to the often quoted MIL-1246C standard that was devised to describe "recently cleaned optics in a cleanroom" [9]; the right one is for a slope of 0.6 which may be more appropriate for telescope optics (cleaning tends to remove more large than small particles, thus raising the slope of the size distribution). Figs. 5–6 in the Appendix show plots of scatter efficiencies as a function of particle diameter. It has to be pointed out that telescope optics are commonly rather dirty, e.g. the VLT mirrors [16], compared to clean room optics in science or industry.

Table 2: Total Integrated Scattering (TIS) and Absorption (TIA) for 1% geometrical area dust coverage. Left: particle size distribution slope 0.926 (MIL-1246 standard), Right: slope 0.6

Band	TIS [%]	TIA [%]	TIS+TIA [%]
R	1.92	0.2	2.12
I	1.97	0.16	2.14
Y	1.95	0.21	2.16
J	1.92	0.26	2.19
H	1.86	0.38	2.24
K	1.76	0.54	2.3
L	1.62	0.78	2.4
M	1.55	0.91	2.46
N	1.31	1.17	2.49
Q	1.23	1.33	2.56

Band	TIS [%]	TIA [%]	TIS+TIA [%]
R	1.57	0.44	2.01
I	1.63	0.38	2.01
Y	1.57	0.45	2.02
J	1.52	0.51	2.03
H	1.42	0.63	2.05
K	1.33	0.75	2.08
L	1.24	0.88	2.12
M	1.22	0.94	2.16
N	1.2	1.05	2.25
Q	1.31	1.06	2.38

Table 2 thus shows that the amount of light removed from the central lobe of the PSF grows with wavelength and can exceed 2.5 times the value expected from geometrical optics. When using a handheld reflectometer to assess the amount of dust on a telescope mirror, as is common practice at ESO and at other observatories, one measures the power of a laser beam reflected on the mirror. It is likely that the measured power is diminished by mirror degradation (e.g., structural/chemical changes within the coating [22]), chemical residues covering the surface such as greasy substances, some of the dust scattering and the dust absorption. The fraction of the dust scattering close enough to the specular direction to enter the pinhole of the reflectometer will be considered unscattered light. Consequently, handheld reflectometers measure TIA plus an unwanted wavelength-dependent fraction of TIS.

When considering thermal emission from a dusty surface, scattering and absorption must be treated separately: The particle emits thermal radiation according to its "grayness" and temperature (which is close to ambient, given that the particle is exposed to air and in thermal contact with the mirror substrate). In addition, there is thermal radiation scattering. When the dome is closed and in thermal equilibrium, the sum of the two equals that of any other part of the telescope. When the dome is opened and the dust is exposed to the cold night sky, thermal scattering will be lowered. One can assign an effective emissivity to the particles of ε_{eff} = TIA / (TIS+TIA). Note that ε_{eff} applies to an effective dust area coverage of TIS+TIA, exceeding the *geometrical* area coverage PAC up to 2.56 times.

Within the ESO-ESA collaboration, there is currently an ongoing activity to measure the BSDF of mirror samples that were exposed to dust in UT3 [8] using commercial scatterometers. From such measurements, one can possibly infer the particle size distribution and then extrapolate the distribution to small scatter angles around specular, which cannot be probed by typical commercial scatterometers.

2. ANALYSIS AND RESULTS

The goal of this report is to analyze and quantify thermal radiation towards the instruments. We begin by going through the three types of thermal radiation listed in Subsection 1.3 in view of the ELT.

2.1 Pupil Geometry

The amount of thermal radiation that arrives on a science detector depends on the cold stop design. Unlike the VLT, the optical stop of the ELT is M1. M1 consists of 798 hexagonally shaped segments.

The segments in the outer rim of M1 have been selected so as to optimally approximate a circular annulus with a diameter of 31 segments. The total glass area amounts to 798 × 1.31 m^2 = 1042.9 m^2. If the pupil cold stops use circular masks and are restricted to an annular all glass pupil with smooth inner and outer rim, the total reflective area is reduced to A_{ann} = 967.5 m^2 = 92.7%.

The inter-segment gaps are 4 mm wide and each segment has a 45° chamfer of 1 mm × 1 mm projected size, hence the distance between the useful reflective areas is 6 mm. The total area of all gaps and chamfers amounts to 9.4 m2, or 0.97% of the pupil area (equivalent to the area of 7.2 segments). We assume that the background behind the gaps is black, hence emits thermal radiation at the dome temperature with emissivity 1. The chamfers, on the other hand, reflect thermal radiation from the dome towards the instrument (when tracing a ray back from the instrument focal plane to an M1 chamfer, the ray would experience a 90° reflection and likely end up somewhere on the inside of the dome, hence a warm location).

ELT instruments that work in the mid-IR, such as METIS, will likely also need to stop out the spider vanes. The six spider vanes have a projected width of 530 mm each, hence in the tight annular of 5544–18486 mm width they cover a total area of 41.2 m^2 = 4.3%, further reducing the effective pupil area to A_{ann} – 41.2 m^2 = 926.3 m^2. The central obscuration has a radius of about 5 m, hence adds a warm area of ~80 m^2 or 8% of A_{ann}.

2.2 Intrinsic Mirror Reflectivity

Figure 3 shows the simulated beginning-of-life coating reflectivity of oxidized aluminium (relevant for all UTs, ATs and the VST), bare silver and the Gemini 4-layer silver recipe [2] versus wavelength. The astronomical bands are again indicated in amber. The model uses standard multi-layer Fresnel equations [19].

A coating roughness of σ = 5 nm RMS is assumed, which has been measured on sputtered silver coatings using atomic force microscopes [18]. This roughness is a property of the sputtering process and not driven by substrate micro-roughness (e.g., ELT M2 polishing spec: σ = 2.5 nm RMS). The Total Integrated Scattering (TIS) due to surface roughness equals TIS = $(2\pi\ \sigma\ \Delta n\ /\ \lambda)^2$, where Δn = 2 for mirrors, hence the intrinsic coating reflectivity is scaled by (1−TIS) [14]. Due to the λ−2 dependence, roughness scattering is mostly relevant for UV.

The dip of the aluminium reflectivity around 825 nm to about 86% reduces the performance in the R, I and Y bands. On the other hand, the reflectivity of the Gemini coating recipe drops sharply below 500 nm, as shown in the inset of Fig. 3. This sudden drop is caused by the protection layer of Si_3N_4 with a thickness of 8.5 nm and the NiCrN adhesion layer. Other coating recipes with better UV reflectivity that approaches, or even exceeds, the reflectivity of bare silver, as shown in Fig. 11.

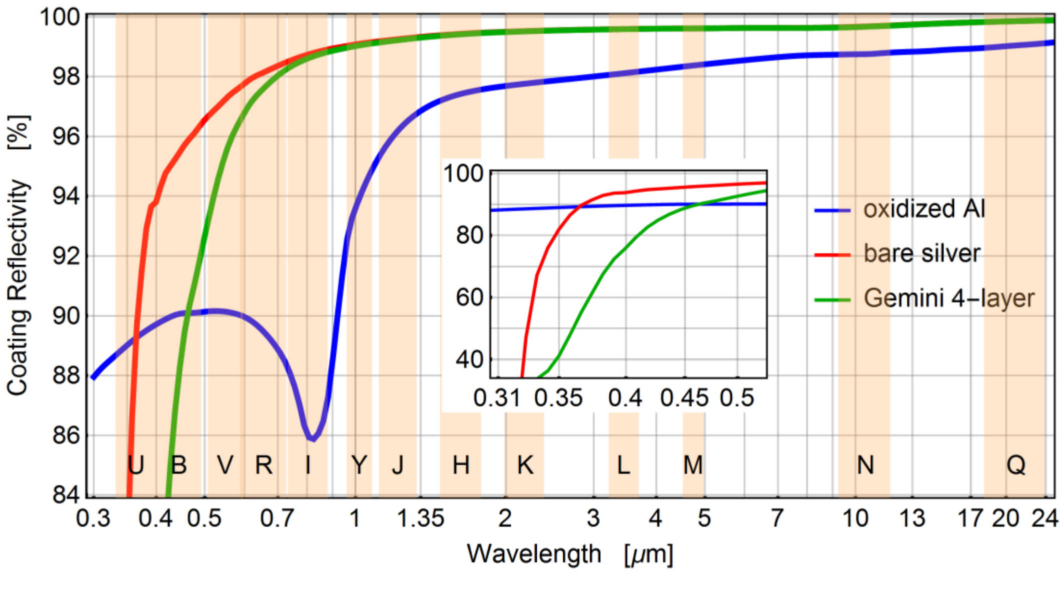

Figure 3. Specular coating reflectivity (simulated single reflection, 10º AOI) of oxidized aluminium (blue), bare silver (red) and the Gemini 4-layer protected silver recipe (green) vs. wave-length across astronomical bands U–Q. The modeled coating micro-roughness is 5 nm RMS.

Figure 4 shows the mirror train reflectivity, hence telescope transmission, of the ELT with baseline coatings. The Gemini silver reflectivity values are taken from measurements on Gemini North M2 witness samples [12] (solid curves) and from simulation (dashed curves). The correct angle of incidence (AOI) has been used for each mirror and, as before, a coating micro-roughness of 5 nm RMS has been modelled. A small dip around 825 nm can be seen since the coating baseline of M4 is aluminium.

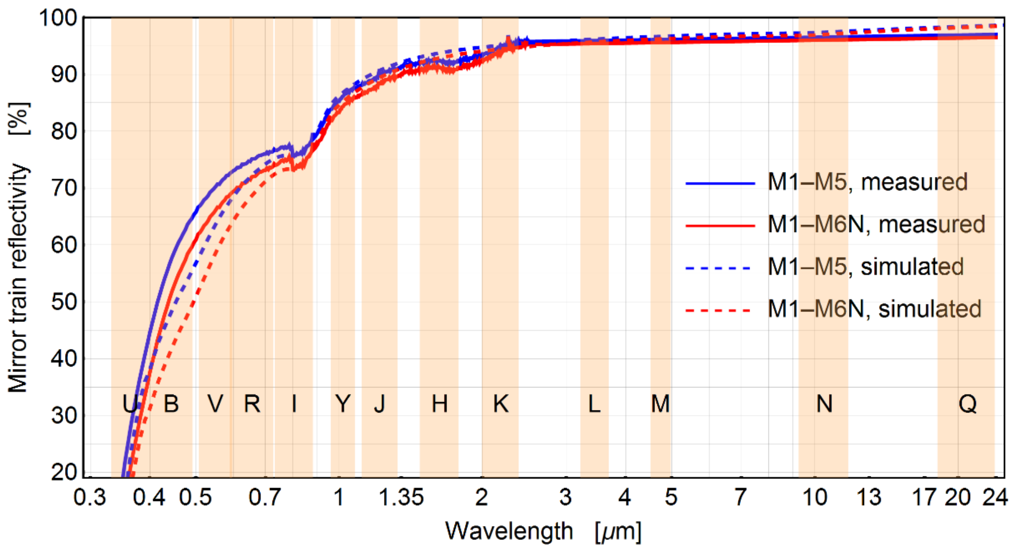

Figure 4. ELT Mirror train reflectivity for M1–M5 (blue) and M1–M6N (red) from [12] and simulation (dashed). The modeled coating roughness is 5 nm RMS.

Table 3 shows in Columns 3 and 4 the band-averaged beginning-of-life reflectivities of a single mirror coated with the Gemini 4-layer recipe and aluminium, respectively. Columns 5 and 6 show the total reflectivity of six subsequent reflections the ELT baseline of M1, M2, M3, M5 and M6 with the Gemini coating and M4 coated with aluminium for M1—M5 and M1—M6 (i.e., the lateral foci), respectively.

Table 3: Specular reflectivity averaged across each band for uncontaminated coatings with 5 nm RMS microroughness (ELT mirror coating baseline: M4 aluminium, all other mirrors Gemini 4-layer protected silver recipe; reflectivity data source: [12])

Band	λ [μm]	single Gemini	single ox. Al	M1–M5 baseline	M1–M6 baseline
U	0.36	71.7	88.	26.3	20.1
B	0.44	89.1	89.2	56.6	50.6
V	0.55	94.	89.6	70.1	65.9
R	0.66	95.8	89.	74.9	71.7
I	0.81	97.1	86.4	76.9	74.7
Y	1.02	97.9	93.7	86.1	84.2
J	1.22	98.3	96.	89.8	88.3
H	1.63	98.7	97.3	92.2	91.
K	2.19	99.2	97.7	94.7	94.
L	3.45	99.5	98.1	96.	95.5
M	4.75	99.5	98.4	96.3	95.8
N	10.5	99.5	98.8	96.7	96.2
Q	21.	99.5	99.	96.9	96.4

According to Eq.(3), the mirror train has an approximate emissivity of $\varepsilon = 1$ – specular reflectivity, amounting for M1–M5 for instance in K-band to $1 - 0.94 = 0.06 = 6\%$ when all coatings are fresh.

In agreement with Fig. 4, the mirror train reflectivity is very good in V-band and higher wavelengths. However, ELT science operation below 400 nm (U-band) is degraded when using the coating baseline in the ELT. Advanced protected silver coatings (not in the baseline) may change this situation; see Fig. 11 for an overview of various mirror coatings.

2.3 Impact of Mirror Contamination

The coating reflectivities diminish over time due to contamination and coating aging (chemical or physical modifications). Contaminants can accelerate the aging, in particular that of (protected) silver coatings, which are prone to tarnishing from the edges and developing pinhole defects. However, reflectometers measure the combined effect of coating degradation, mirror roughness and dust and those effects cannot be differentiated in this analysis.

An estimate of the ELT dust coverage is provided in Section 3.3 of [1], quote:

> With the baseline of recoating M1 segments every 18 months, the time averaged segment dust exposure is 548/2 = 274 days = 9 months → 4.1% reflectivity loss. Assuming that the other mirrors are cleaned/recoated every 24 months (→365 days avg. exposure), we experience a time average of 14.1% telescope specular reflectivity loss, and thus emissivity increase, due to dust (equivalent to "7 times CL630")

Reflectivity non-uniformity will lead to diffraction speckles in the AO-corrected telescope PSF, limiting performance in high-contrast imaging and jeopardizing in particular exoplanet detection capabilities (see e.g. Fig.6 in [15]).

Requirement I-INS/ELT-185 in the ELT Common ICD to the Instruments [20] specifies:

> The transmission non-uniformity across the pupil, not taking into account missing segments, shall be better than 10% peak to valley (TBC).

With the current recoating baseline, the lateral reflectivity variation from contamination on M1 alone would be $2 \times 4.1\% = 8.2\%$ PtV. It is difficult to determine how much transverse variability is added by the other mirrors. Presumably, M3 has the largest contribution among the remaining mirrors since it is optically conjugated still rather close to the pupil and it faces upward. Since the non-uniformity of 8.2% PtV of M1 alone is already close to 10%, it cannot be easily determined if the requirement will be met or not.

2.4 Quantifying TSE

The key sections of the ELT Common ICD related to TSE are INFO-INS/ELT-196, -197 and -198, which are copied below:

> **INFO-INS/ELT-196:** With a full-sized cold stop including the central obscuration and a spider mask the thermal self-emission was calculated to be 12.8% for perfectly clean mirrors and 23% for the CL630 (1% dust coverage) condition. The main terms contributing to the clean mirror TSE are mirror emissivity, segment gaps (0.71%), missing glass at the edge of the pupil (0.94%).
>
> For the case of 1% dust coverage additional terms contributing to the TSE include the higher emissivity of the mirror surfaces and thermal light scattered into the optical path.
>
> **INFO-INS/ELT-197:** With a full-sized cold stop including the central obscuration and excluding a spider mask the thermal self-emission was calculated to be 16.7% for perfectly clean mirrors.
>
> **INFO-INS/ELT-198:** With a full-sized cold stop excluding the central obscuration and excluding a spider mask the thermal self-emission was calculated to be 36.1% for perfectly clean mirrors.

In Section 2.1, we find a total area of all gaps and bevels of 1% (including a missing segment or two). The baseline pupil misses 1% reflective area on the outer rim of M1 and radiates accordingly. According to Section 2.2 and the second last column in Table 3 (baseline M1–M5 coating), the emission due to (fresh) coating absorption is 1 − 0.861 = 13.9% at the most above 1 μm (i.e., Y-band and larger wavelengths) and 5.3% above 2 μm (i.e., K-band and larger wavelengths). Accumulated dust on M1–M5 adds 14.1% emissivity, averaged over time (however, this contamination level is different from CL630, hence it is difficult to compare with the Common ICD). The combined TSE for average contamination is then 13.9% + 14.1% = 28%.

If the cold stop mask does not mask the spider, another 4.3% emissivity is added, then totalling 13.9% + 1% + 1% + 4.3% = 20.2%. Finally, if on top of the spider also the central obscuration is not masked, further 8.2% warm area must be added to the pupil for a total of 20.2% + 8.2% = 28.4%.

3. CONCLUSIONS

This report contains an analysis of thermal self-emission (TSE) in the ELT. It is part of a set of stray light analyses, corresponding to different aspects as indicated in Fig. 1, see also [1]. The results presented here have not been derived using raytracing software such as FRED or Zemax, but instead are based on analytical calculations and data from *SkyCalc*.

The importance of TSE suppression varies strongly with the astronomical case and the spectral range. In general, AO-assisted observations in the infrared requiring high contrast, and thus high SNR, such as imaging planets around solar-like stars in reflected light, profit the most from TSE.

The expected TSE for different assumptions regarding the mirror contamination level and type of cold stop is provided in Section 2.

The largest potential for reducing thermal emissivity of the ELT during operations lies in employing high-quality protected silver coatings and applying frequent (in-situ) cleaning to the mirrors, in particular the upward facing ones (M1, M3, M5). Furthermore, it is advisable that the instruments working in the infrared employ cold stops which cover the central obscuration and, if possible, also the spider (the latter requires that the cold stop stays fixed with the telescope and does not rotate with the sky).

Covering the M2 spider and possibly part of the Top Ring with selective foil that is black in the visible, but highly reflective (and thus has low emissivity) in the infrared starting in K-band, would reduce sky cooling of the telescope structure, thus reducing structural stress due to temperature gradients and mitigating spider seeing (the so-called low-wind effect) [21]. Furthermore, when applied to the underside of the AR Tower spider (which lies in the shadow of the M2 spider), it reduces the thermal radiation seen by any instrument whose cold stop does not mask the spider vanes.

4. APPENDIX

This Appendix provides additional information on Mie scattering on dust particles. Figure 5 shows phase functions and scatter efficiencies at 658 nm = R-band center for a lognormal particle size distribution. The upper row is for a distribution slope is for the slope of 0.926, as specified by the MIL-1246 standard and its international equivalent [9], and the bottom row for a slope of 0.6. The MIL-1246 standard was first released in the 1960s to characterize dust particle sizes of "recently cleaned optics" in US military cleanrooms. Since cleaning removes more large than small particles, the slope is quite steep. Conversely, for mirrors exposed to the open air that are not cleaned frequently, as in terrestrial telescopes, a shallower slope like 0.6 is more appropriate, raising the fraction of larger particles. It is unclear how cleaning with CO_2 snow influences the slope, but likely the effect is similar.

The phase function is a measure of scattering efficiency of a dust ensemble whose particles are randomly distributed in 3D space, e.g. diluted airborne dust. The curve is strongly peaked along the direction of forward scattering (small angle between incident and scattered rays; note the logarithmic scale). The lower left curve is steeper than the upper left one because large particles (slope 0.6) preferentially scatter in small angles. Near 180° (backscattering), there are two small peaks.

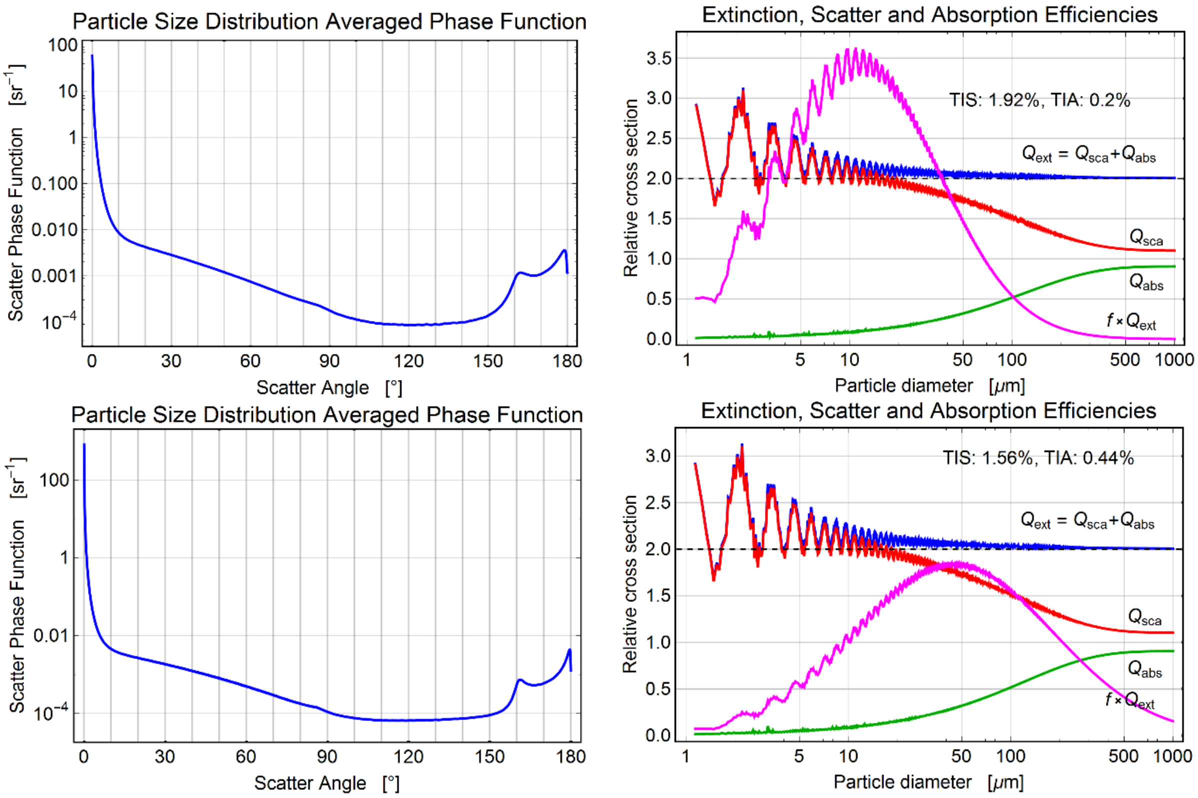

Figure 5. Left column: Mie scattering phase functions at 658 nm = R-band, averaged over a lognormal particle size distribution (upper row: slope 0.926 as in the MIL-1246 standard, bottom row: slope 0.6), Right column: Relative scatter and absorption cross sections pertaining to the two phase functions.

The right column shows the scatter and absorption cross sections in units of the geometrical projected cross section of the particles. In the limit of large particles compared to the wavelength, the extinction efficiency Q_{ext}, defined as the sum of elastic scattering Q_{sca} and absorption Q_{abs} (blue curve), converges exactly to 2, eventually consisting in equal parts of scattering and absorption, a somewhat counter-intuitive result known as the Extinction Paradox [3].

The pink curve shows the quantity $f \times Q_{ext}$, where f is the particle number density in a given particle size bin; hence this curve indicates which size particles actually scatter or absorb most of the light within a distribution. The peak near 10 μm in the upper right plot (slope 0.926) shifts towards 50 μm in the lower right plot (slope 0.6). The corresponding values of TIS (Total Integrated Scattering) and TIA (TI Absorption) are indicated in the plots. Different particle size distributions at the same geometrical area coverage thus can have different emissivity.

Figure 6 shows the same as Fig. 5, but for a slope of 0.6 and wavelengths of 2.2 μm = K-band (upper row) and 10.5 μm = N-band (bottom row). The phase function peak softens with increasing wavelength. The extinction Q_{ext} oscillates and reaches a maximum of up to 4 for particle sizes near the wavelength.

In order the derive the BSDF (Bidirectional Scatter Distribution Function) for particles on a (reflective) surface, one sums the phase function with a reversed and shifted version of itself in order to model directly (unreflected) scattered radiation and scattered radiation that reflects off the mirror. This function is then multiplied by correction terms to account for the obliquely projected area coverage on the 2D surface and to enforce energy conservation [10].

Examples for Mie scatter BSDF curves for MIL-1246 produced by FRED are displayed in Fig. 7 for 551 nm (center of V-band, top two plots) and 2.2 μm (K-band, bottom two plots) versus linear scatter angle θ (first and third plot) and versus distance from the specular ray direction $|B{-}B_0|$, where $B = \sin(\theta)$, in double-logarithmic scale.

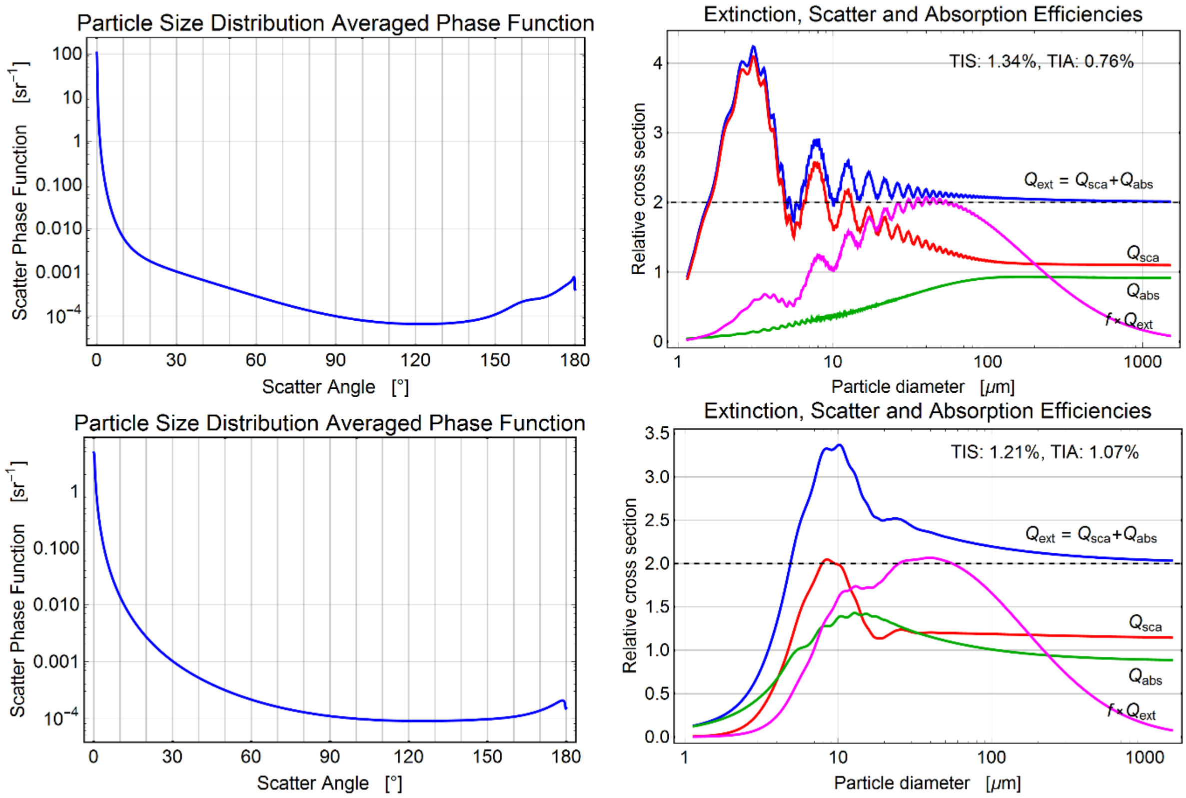

Figure 6. Left column: Mie scattering phase functions, averaged over a lognormal particle size distribution at slope 0.6 (upper row: 2.2 µm = K-band, bottom row: 10.5 µm = N-band), Right column: Relative scatter and absorption cross sections pertaining to the two phase functions

The latter plotting method zooms in on the near specular angle range, where the curves level off at about 30 arcminutes, albeit at very high scatter efficiencies. This regime is relevant for in-field scattering in telescopes, e.g. for high-contrast imaging, but it is inaccessible to typical commercial scatterometers. When using measured BSDF curves, one therefore has to extrapolate below about 0.5° scatter angle from specular by fitting to simulated (Mie) BSDFs. The different color curves in the plot correspond to different angles of incidence ("ANG").

Note that high-contrast imaging observations strongly profit from even superficial cleaning such as with CO_2 snow (large particle removal). Large particles, scratches and possibly sharp segment chamfers edges can produce strong small-angle scattering.

It is evident that the BSDF peak around the specular direction broadens with increasing wavelength. Hence, mechanical parts in an optical system, such as a mirror cell rim or a spider, scatter over much larger angles in the thermal IR than in the visible. Consequently, it makes sense to coat surfaces close to telescope optics with a material that reflects well in the thermal infrared such as polished aluminium.

If a warm part lies inside the pupil, as e.g. the earthquake retainer brackets above the VLT primary, it can make sense to cover them with mirrors as shown in Fig. 8. These mirrors are a few centimeters out of focus in order not to produce sharp ghost images of the areas on sky they are pointing at. On the other hand, they can raise the apparent sky background in the visible, in particular when the telescope is pointing at a bright region such as the Galactic Center. Optimally, one would use a coating material that is reflective in the thermal IR, but black in the visible. A foil that approximates this behaviour is produced by Acktar under the name *NanoBlack*, as detailed in Section 2.3.

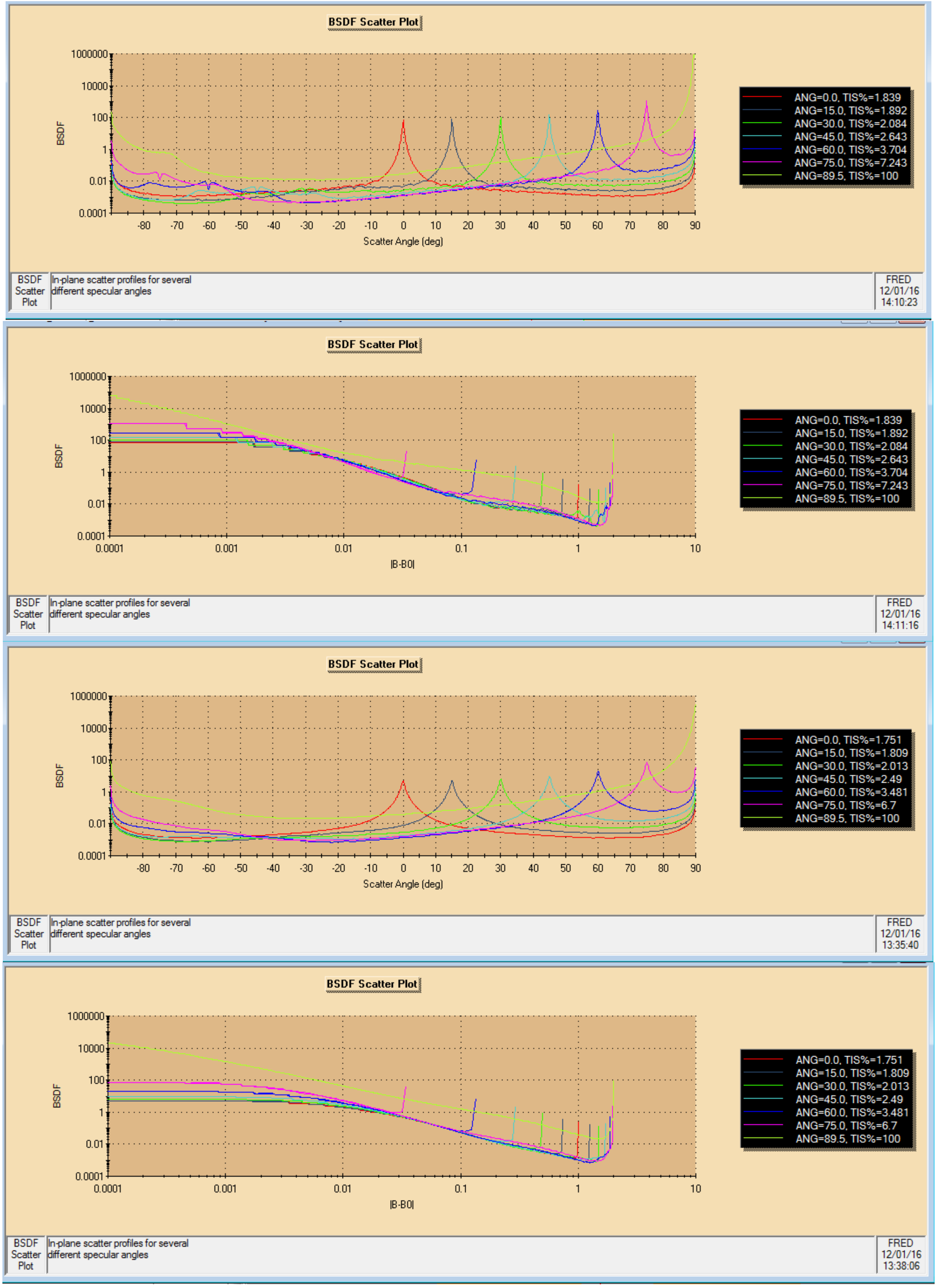

Figure 7. BSDF plots from FRED for 551 nm (V-band, top 2) and 2.2 μm (K-band, bottom 2) vs. linear scatter angle and off-specular scatter angle $|B-B_0|$ (FRED is an optical modeling application produced by Photon Engineering, LLC)

Figure 8. Left: Photo of the M1 rim with mirror cell in UT1, Right: Detail with two mirrors covering the earthquake retainer clamps in order to reduce pupil emissivity (photo: S. Guisard)

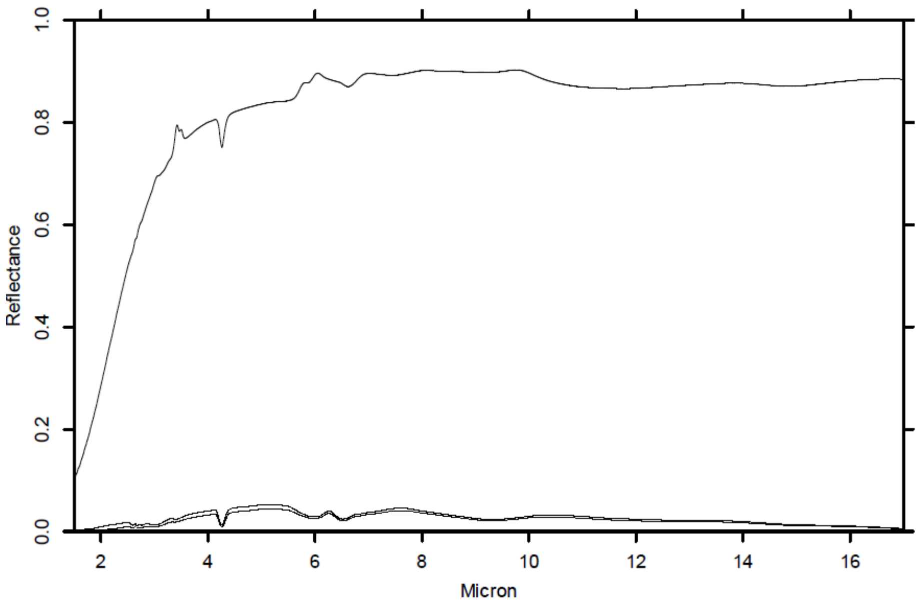

Figure 9. Spectral reflectance of Acktar *NanoBlack* foil (top curve; Source: ACM Coatings/Acktar)

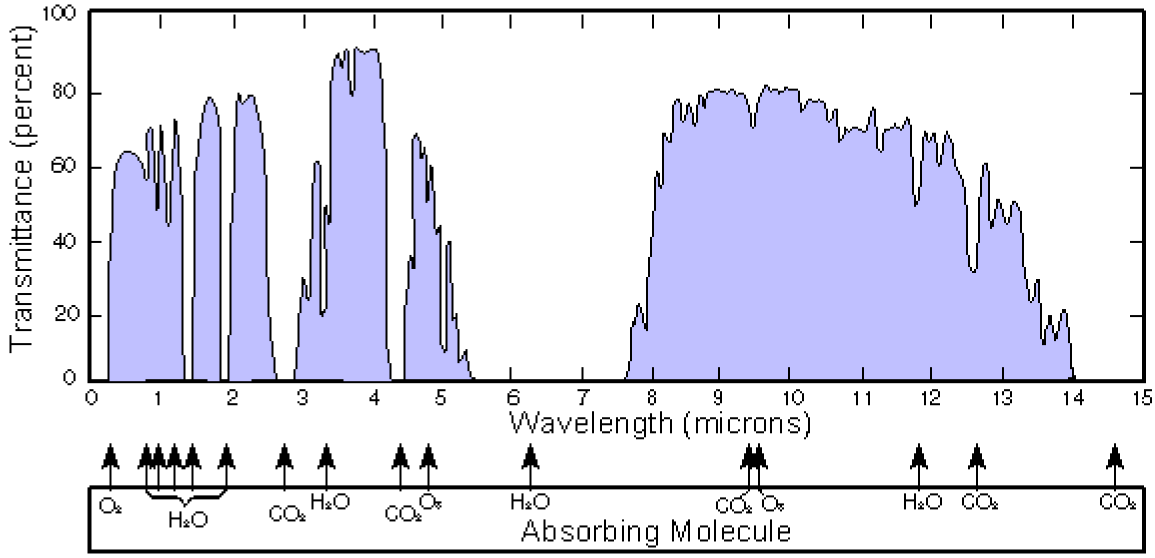

Figure 10. Atmospheric transmission and absorption bands

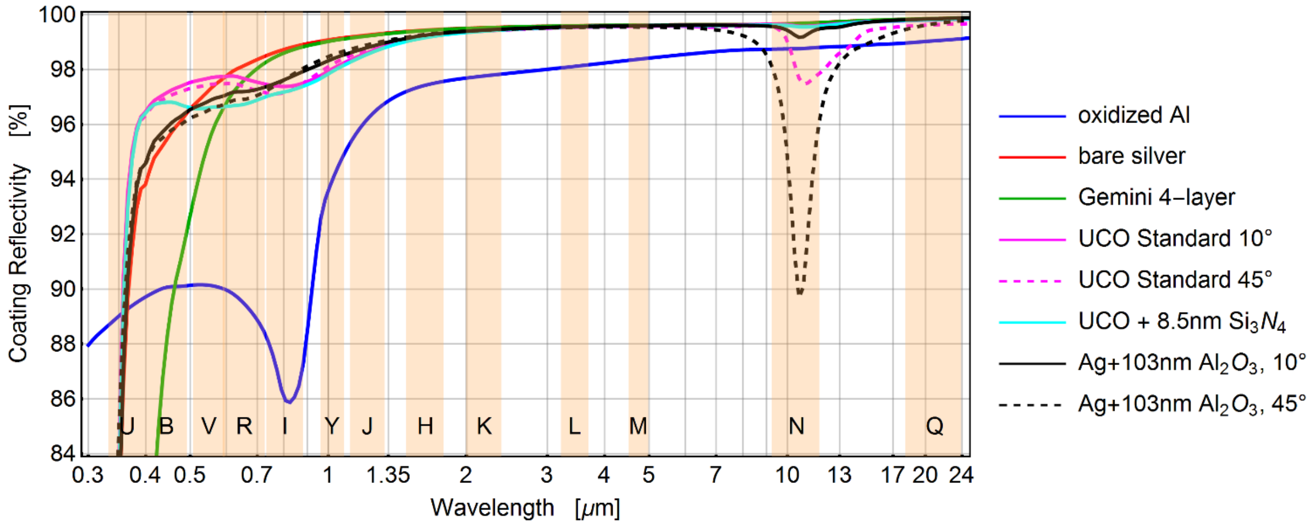

Figure 11. Reflectivity of various coatings (simulated single specular reflection, 10º AOI unless stated otherwise). The modeled coating roughness is 5 nm RMS. The “UCO Standard” silver coating is described in [11]

REFERENCES

[1] Holzlöhner, R. "Towards a Stray Light Analysis of the ELT", Proc. AO4ELT5 (2017), DOI: 10.26698/AO4ELT5.0138

[2] Boccas, M.; Vucina, T.; Araya C.; *et al*.," Coating the 8-m Gemini telescopes with protected silver", Proc. SPIE 5494 (2004)

[3] Bohren, C. F. and Huffman, D. R., *Absorption and Scattering of Light by Small Particles*, Wiley (1983)

[4] Berdahl, P. and Martin, M., "Emissivity of Clear Skies", Solar Energy **32**, p.633 (1984)

[5] Brewster, M. and Quinn, *Thermal Radiative Transfer and Properties*. John Wiley & Sons (1992)

[6] Goforth, M. A., Gilcrest, G. W., Sirianni, J. D., "Cloud Effects on Thermal Downwelling Sky Radiance", Proc. SPIE **4710** (2002)

[7] Greve, A. and Bremer, M., *Thermal Design and Thermal Behaviour of Radio Telescopes and their Enclosures*, Springer, Dordrecht (2010)

[8] Guisard, S. "Study of the effect of dust deposition on Paranal mirrors – Report 2014", Internal ESO draft report (2014)

[9] IEST-STD-CC1246D Product Cleanliness Levels and Contamination Control Program

[10] Jenkins, D. G.; Fest, E.C.; Kremer, R.M. and Spyak, P.R., "Improved Mie theory scatter model for particulate contamination that conserves energy and obeys reciprocity", Proc. SPIE **6291**, 62910Q (2006)

[11] Phillips, A. C. "Progress in UCO's search for silver-based telescope mirror coatings", Proc. SPIE **8450** (2012)

[12] Schneider, T. Table of measured spectral reflectivity on protected silver Gemini North M2 witness samples, June 2018 (private communication)

[13] *SkyCalc*, Online ESO exposure and sky background calculator, <https://www.eso.org/observing/etc/skycalc/>

[14] Stover, J.C., *Optical Scattering Measurements and Analysis*, SPIE Press, 3rd Ed, ISBN: 9781628418408 (2012)

[15] Troy, M., Crossfield, I. Chanan, G. *et al*., "Effects of diffraction and static wavefront errors on high-contrast imaging from the thirty meter telescope," in Advances in Adaptive Optics II, Proc. SPIE **6272**, 62722C (2006)

[16] Vogt, F. P. A. *et al*., "Laser-induced Raman scattering in astronomy: the impact of dusty telescope mirrors", Astron & Astrophys, in preparation

[17] Vucina, T.; Boccas, M.; Araya, C.; Ahhee, C., "Gemini's protected silver coatings: first two years in operation", SPIE **6273**, 62730W (2006); doi: 10.1117/12.670866

[18] Webb H. K., "Roughness Parameters for Standard Description of Surface Nanoarchitecture", J. Scanning Microsc. **34**, pp.257–263 (2012)

[19] Azzam, R. M. A. and Bashara, N. M., *Ellipsometry and Polarized Light*, North-Holland (1977)

[20] "Common ICD between the ELT Nasmyth Instruments and the Rest of the ELT System", ESO-253082 Iss.3, ESO document (Nov. 2017)

[21] Sauvage, J., Fusco, T., Guesalaga, A., Wizinowitch, P., O'Neal, J., N'Diaye, M., *et al*., "Low Wind Effect, the main limitation of the SPHERE instrument", Conf. Proc. AO4ELT4, 1(1) (2015)

[22] Folgner, K. A., *et al.* "Environmental durability of protected silver mirrors prepared by plasma beam sputtering", Appl. Opt. **56**, C75–86 (2017)